Research

Author for correspondence:
Douglas H. Kelley
e-mail: d.h.kelley@rochester.edu

Perivascular pumping of cerebrospinal fluid in the brain with a valve mechanism

Yiming Gan[1], Stephanie Holstein-Rønsbo[2], Maiken Nedergaard[2,3], Kimberly A. S. Boster[1], John H. Thomas[1] and Douglas H. Kelley[1]

[1]Department of Mechanical Engineering, University of Rochester, Rochester, NY 14627, USA
[2]Center for Translational Neuromedicine, University of Copenhagen, Copenhagen, Denmark
[3]Center for Translational Neuromedicine and Department of Neuroscience, University of Rochester Medical Center, Rochester, NY 14627, USA

YG, 0000-0002-2463-6316; KASB, 0000-0001-5178-128X; JHT, 0000-0002-7127-8654; DHK, 0000-0001-9658-2954

The flow of cerebrospinal fluid (CSF) along perivascular spaces (PVSs) is an important part of the brain's system for clearing metabolic waste. Experiments reveal that arterial motions from cardiac pulsations and functional hyperae-miadrive CSF in the same direction as the blood flow, but the mechanism producing this directionality is unclear. Astrocyte endfeet bound the PVSs of penetrating arteries, separating them from brain extracellular space (ECS) and potentially regulating flow between the two compartments. Here, we present two models, one based on the full equations of fluid dynamics and the other using lumped parameters, in which the astrocyte endfeet function as valves, regulating flow between the PVS and the ECS. In both models, cardiac pulsations drive a net CSF flow consistent with prior experimental observations. Functional hyperaemia, acting with cardiac pulsation, increases the net flow. We also find, in agreement with experiments, a reduced net flow during wakefulness, due to the known decrease in ECS permeability compared to the sleep state. We present *in vivo* imaging of penetrating arteries in mice, which we use to measure accurately the amplitude of their constrictions and dilations during both cardiac pulsation and functional hyperaemia, an important input for the models. Our models can be used to explore the effects of changes in other input parameters, such as those caused by ageing or disease, as better measurements of these parameters become available.

1. Introduction

The annular perivascular spaces (PVSs) surrounding blood vessels in the brain cortex provide low-resistance pathways that carry cerebrospinal fluid (CSF) into the brain, promoting clearance of metabolic wastes (see recent reviews [1,2]). Experiments reveal that CSF in pial (surface) arterial PVSs flows in the same direction as the blood flows, while also pulsing at the cardiac frequency [3–5]. However, the driving mechanism is poorly understood. This pulsatile flow, with a net (bulk) flow, has been attributed to *peristaltic pumping* [6] by arterial cardiac pulsations, in which peristalsis drives a net flow in the same direction as the arterial wall wave [7,8]. However, the wavelength of the arterial pulsations is approximately 1 m, far greater than the length of arteries in the brain (approx. 1 mm in mice). In such a sub-wavelength domain, the peristaltic pumping mechanism alone likely does not drive CSF flow at the speeds observed in experiments, approximately 20 μm s^{-1} in pial PVSs of mice [9,10].

Functional hyperaemia, the increase of blood flow to neurologically active brain regions, has also been shown to propel CSF flow [11]. Functional hyperaemia is associated with artery dilations of longer time scale and larger amplitude (approx. 10 s, 10%) compared to cardiac pulsations (approx. 0.3 s, 2%). The mechanism by which functional hyperaemia promotes CSF influx is not well understood. Kederasetti *et al.* [12] considered a poroelastic model that couples the axial flow along the PVS of a penetrating cortical artery and

a radial flow between the PVS and the extracellular space (ECS). Their model suggests that functional hyperaemia with a temporally asymmetric waveform of arterial pulsation can drive a net radial flow from the PVS into the ECS. Holstein-Rønsbo *et al.* [13] observed increased tracer influx and clearance during functional hyperaemia in mice, and they proposed impedance pumping as a possible mechanism. In their model, constructive and destructive interference of waves reflected between PVS bifurcations and other features drives a net flow.

A possible mechanism for producing bulk motion of CSF into the brain is the presence of valves or valve-like structures. While no valves have been found inside the PVSs themselves, the outer boundary of a PVS of a penetrating artery, formed by astrocyte endfeet, is a possible candidate. Indeed, Bork *et al.* [14] recently proposed a mechanical model of flexible endfeet in which a fluctuating pressure causes the endfeet to flap in a way that promotes a directional flow, similar to the action of a bicuspid valve. Several studies using extracellular tracers indicate that fluid communication between PVSs and the ECS occurs mostly through the gaps between endfeet (see the reviews [1,15,16]). (It has also been suggested that some communication occurs through the astrocyte bodies themselves [17].) Other studies proposed that astrocyte endfeet act as valves controlling the resistance to axial flow, resulting in backflow in the nanomembrane to the brain surface under functional hyperaemia [18,19], although the mechanism for controlling the resistance was not defined.

Here, we propose that astrocyte endfeet act as valves, with the fluid permeability of the endfoot layer increasing whenever the pressure in the PVS exceeds the pressure in the ECS. We focus on the implications of this hypothesized valve action for CSF flow, not on the mechanics of how the valves themselves operate. However, the scenario we consider here is consistent with the recent mechanical model of an endfoot valve proposed by Bork *et al.* [14]. Our model is also consistent with a related proposed mechanism in which dilation of a penetrating artery causes an outward deformation of the outer boundary of its PVS [20,21]: we would expect the endfoot gaps to expand when the artery dilates, increasing the permeability, and shrink when the artery constricts, reducing the permeability. This pressure-dependent permeability could explain how pulsatile CSF motion is rectified to produce a net flow in the same direction as the blood flow in a penetrating PVS. During artery dilation, the PVS shrinks, requiring fluid to be expelled, and increased permeability of the endfoot wall allows fluid to pass into the ECS. During artery constriction, the PVS expands, requiring fluid intake, and reduced permeability of the endfoot wall inhibits a reflux of fluid from the ECS, so the fluid must come instead from the pial PVS connected to the penetrating PVS.

Our proposed valve mechanism can also explain how wakefulness suppresses CSF influx. During wakefulness, the permeability of the ECS is lower by a factor of five than during sleep [22]. Although cardiac pulsations and functional hyperaemia occur in both states, CSF inflow in the PVSs is rarely observed during wakefulness. Solute measurements show that perivascular CSF tracer influx and interstitial solute efflux, including the clearance of amyloid beta, are more rapid in the sleeping brain compared to the awake brain [22]. Few theories of perivascular pumping consider how wakefulness suppresses CSF inflow, or whether ECS permeability is responsible, as they do not include an

exchange of fluid between the PVS and the ECS. Because the astrocytic valves we model here control the net CSF flow transport into the ECS, it is natural to expect that the decreased permeability of the ECS during wakefulness will suppress the valve mechanism.

In this study, we use the lubrication approximation to simulate the CSF flow in the PVS of a cortical penetrating artery caused by arterial motions. The analysis is similar to that of Romanó *et al.* [20]. The PVS is considered to be an open, unobstructed space, and the outer wall of the PVS (the endfoot wall) is permeable to CSF and deformable. We set the permeability of the outer wall to be a step function of the pressure in order to model the valve function [19]. We couple the CSF flow in the PVS with the pressure response in the ECS, which is modelled as a porous medium. We find that both cardiac pulsations and functional hyperaemia drive a net CSF flow from the the upstream pial PVS into the penetrating PVS. During wakefulness, our model displays a higher ECS pressure response and a suppression of the CSF inflow. We further simplify our model by employing lumped parameters to gain a comprehensive understanding of the pumping mechanism, considering varied arterial-pulsation frequencies and endfoot wall elasticities.

An important input to our models is the amplitude of the arterial pulsations. Measurements of CSF flow and arterial pulsations have been generally limited to the PVSs of pial arteries because the PVSs of penetrating arteries are difficult to image. Studies have shown, however, that penetrating arteries have larger pulsatility than the mother pial artery [23,24], which would enhance the pumping with the proposed valve mechanism. Here, we use robust *in vivo* imaging techniques and custom-written processing software to measure the cardiac pulsations of penetrating arteries of mice. We also use whisker stimulation to activate functional hyperaemia and measure the associated diameter changes [13].

2. The model

Here, we describe the idealized computational model of our proposed valve mechanism. Details of the governing equations and numerical methods, based on those of Romanò *et al.* [20], are described in appendix B. We model the flow of CSF in two connected, axisymmetric domains, as shown in figure 1*a*. The PVS of a penetrating artery is modelled as a circular annular tube of length l and width b, lying between the impermeable, deformable artery and the permeable, deformable endfoot wall. The width of the PVS is taken to be $b = 10\,\mu m$, the radius of the artery is taken to be $r_1 = 10\,\mu m$, and the length is taken to be $l = 1000\,\mu m$, typical values for a penetrating artery in the mouse brain [25]. (Values of all of the dimensional parameters of the model are listed in table 1.) The PVS is an open space [26,27], and the flow there obeys the Navier–Stokes equation, in its approximate form for low Reynolds number flow in a thin tube (the lubrication approximation) and quasi-steady flow (low Womersley number). The aspect ratio of the PVS, $\varepsilon = b/l$, is of order 0.01, justifying the use of the lubrication approximation.

At the inlet (the upstream pial PVS) and the outlet (a precapillary PVS) we specify a hydraulic resistance to model the inflow and outflow and require conserved flow rates across each interface. The inner boundary of the PVS (the artery wall) is assumed to be impermeable, and we apply a no-slip
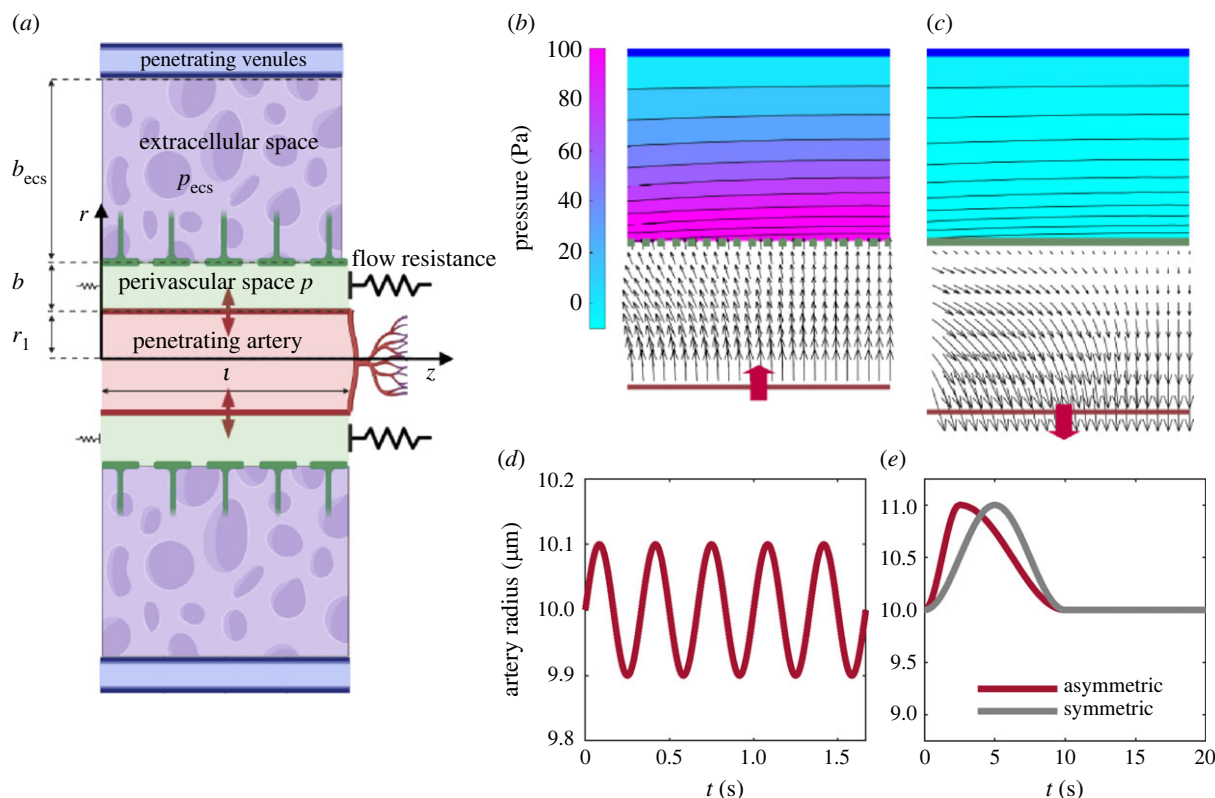
Figure 1. Sketch of the model. (a) The model includes the exchange of cerebrospinal fluid (CSF) between the perivascular space (PVS) of the artery, modelled as an open space, and the extracellular space (ECS), modelled as a porous medium. The upstream PVS of the pial artery and the downstream PVS of a capillary are modelled as flow resistances. (b) During artery dilation, hypothesized astrocytic valves along the PVS outer boundary open, facilitating flow into the ECS, which increases the ECS pressure. (c) During artery constriction, astrocytic valves close. The constriction drives CSF flow in the PVS and decreases ECS pressure. (d) The arterial radius varies during cardiac pulsation according to equation (2.2). (e) The asymmetric ($n = 2$) and symmetric ($n = 1$) arterial waveforms of functional hyperaemia generated by equation (2.3).

boundary condition there. The outer boundary of the PVS (formed by the astrocyte endfeet) is modelled as a thin, deformable, elastic layer of permeable tissue, with a no-slip boundary condition. The Young's modulus of this elastic layer, E_{endft}, lies in the range $[10^4\ 10^6]$ Pa [20]. To represent the proposed valve mechanism, the permeability k_{endft} of the outer boundary of the PVS is modelled as a step function of the pressure difference:

$$k_{endft} = \begin{cases} k_1 & \text{if } p(z, t) > p_{ecs} \\ k_0 & \text{if } p(z, t) \leq p_{ecs} \end{cases} \quad (2.1)$$

where $k_1 > k_0$ and $k_0 = 10^{-10}$ m Pa^{-1} s^{-1} [28]. Thus, during artery dilation, the increased pressure in the PVS increases the permeability, effectively opening a valve and allowing fluid to enter the ECS (figure 1b). During artery constriction, the pressure in the PVS drops, permeability is decreased, the valve closes, and CSF flow is confined to the PVS (figure 1c).

The ECS surrounding the PVS is modelled as a large porous, circular annular tube of length l and width b_{ecs}, filled with a porous medium composed of a deformable but incompressible solid phase and an incompressible fluid phase (interstitial fluid) that flows according to Darcy's law. The annular width of the ECS, b_{ecs}, is taken to be a typical distance to the nearest venule, which is 100 µm for the mouse brain [25,29]. The permeability of the ECS during wakefulness has been measured as $[2 \times 10^{-17}$ m^2 1×10^{-16} m^2] [30–32]. To model sleep, we set the permeability to its maximum value, $k_{ecs} = 1 \times 10^{-16}$ m^2, about five times greater than the value we use to model wakefulness [22]. The flow velocity is kept continuous across the outer boundary of the PVS, where it meets the endfoot wall and the ECS. The pressure difference across this boundary

depends on both the elasticity of the thin membrane and the flow rate through it, as described in appendix B. The fluid pressure is set to zero at the outer boundary of the ECS. The fluid axial pressure gradient is set to zero at the distal and proximal ends of the ECS in z direction.

The motion of the impermeable artery wall is specified as an input, representing cardiac pulsations or functional hyperaemia. Given that the wave speed of arterial pulsations is of order $c \approx 1$ m s^{-1}, the cardiac frequency is $f \approx 3$ Hz, and the length of the domain is $l = 1000$ µm, we have $lf/c \approx 0.003$, and hence we can neglect the phase difference in the pulsations along length of the tube. (This phase difference is also negligible for the slower arterial motions associated with functional hyperaemia.) Thus we model the cardiac pulsations as

$$h(t) = h_{cp} \sin(2\pi f t) \quad (2.2)$$

(figure 1d), independent of the axial coordinate z. h_{cp} is the pulsation amplitude. For functional hyperaemia, we model an individual pulsation as a quick dilation followed by a slow constriction and relaxation, in the form

$$h(t) = \begin{cases} \frac{h_{fh}}{2}(1 - \cos(2n\pi f t)) & \text{if } t \leq \frac{1}{2nf} \\ \frac{h_{fh}}{2}\left(1 - \cos(2(\frac{1}{2-(1/n)})\pi(ft-1))\right) & \text{if } \frac{1}{2nf} < t \leq \frac{1}{f} \\ 0 & \text{if } t > \frac{1}{f} \end{cases}$$

$$(2.3)$$

with $f \approx 0.1$ Hz, where h_{fh} is the dilation amplitude, and n determines the fraction of dilation time and constriction time. We use $n = 1$ to model temporally symmetric vasomotion and $n = 2$ to model temporally asymmetric vasomotion.

Table 1. Dimensional parameters.

u	axial CSF velocity	
w	radial CSF velocity	
r	radial coordinate	
z	axial coordinate	
t	time	
p	pressure in the PVS	
q	axial flow rate in the PVS	
f	the arterial pulsation frequency	
μ	dynamic viscosity of CSF	9×10^{-4} Pa s^{-1}
r_1	artery radius	10 μm
l	length of the penetrating artery	1000 μm
h_{cp}	artery pulsation amplitude of the cardiac pulsation	$*[0.01r_1, 0.025r_1]$
h_{fh}	artery dilation amplitude of functional hyperaemia	$*[0.1r_1, 0.2r_1]$
h	arterial waveform of cardiac pulsation or functional hyperaemia	
b	width of the PVS	10 μm
a_{pvs}	equilibrium cross-sectional area of the PVS	942 μm^2
E_{endft}	elasticity of the PVS outer boundary	$*[10^4, 10^6]$ Pa
k_{endft}	permeability of the PVS outer boundary	10^{-10} m Pa^{-1} s^{-1}
k_{pial}	conductivity of the pial PVS	1000 $k_{endft}a_{pvs}$
k_{cap}	conductivity of the capillary PVS	$k_{endft}a_{pvs}$
k_{ecs}	permeability of the ECS	$*[2 \times 10^{-17}, 10^{-16}]$ m^2
b_{ecs}	width of the ECS domain/distance between the artery and the venules	10^{-4} m
u^*	axial CSF velocity relative to the endfeet motion	

In both cases, the waveform is smooth, with a continuous wall velocity (figure 1*e*).

3. Experimental measurements of penetrating artery motions due to cardiac pulsations and functional hyperaemia

The pulsation amplitude of a penetrating artery is a vital input for our model. However, compared to the surface pial arteries, experiments for penetrating arteries are limited. Fast line scans provide high temporal resolution [23,24,33] but are sensitive to errors in image registration. A slight shift in the cross-sectional plane, perhaps due to motion artefacts during an experiment, can cause a large variation in the measurement. Here, we present 2-photon recordings of the cross-sectional plane of the penetrating artery.

In the experiments, mice were head-plated and a cranial window was carefully inserted above the middle cerebral artery (MCA) under ketamine/xylazine anaesthesia, before transferring the mice for 2-photon *in vivo* imaging. Before imaging, an intravascular tracer (0.1 ml FITC-labelled 2000 kDa dextran, 1%; Sigma-Aldrich, FD2000S) was injected in order to visualize the artery. A penetrating branch of the MCA was located, and unilateral whisker stimulations [13] were applied to record arterial diameter changes. Imaging was performed just below the cortical surface (at 0 μm) and 100 μm deeper. We alternated between the upper and lower depth (five stimulations each). The imaging was performed at 128×128 pixels, 4× zoom, 59 or 113 frames per second. More details of the experiments are given in appendix A.

To measure the area change of the artery over time, we used a custom segmentation code that is insensitive to the artefacts of in-plane shifts (figure 2*d*). Since the cross section of the penetrating artery is essentially circular, we can calculate an effective diameter $d = 2(A_{artery}/\pi)^{1/2}$, where A_{artery} is the measured area (figure 2*b,e*).

It has been reported that a penetrating artery has pulsatility that increases from the surface to deeper brain regions [23,24]. To confirm this, we compared observations at depths 0 μm and 100 μm. When observing pulsation due to the cardiac cycle, we applied a bandpass filter in the range 2 Hz to 6 Hz to the diameter signal (figure 2*b* shows 5 s of the signal). The pulsation percentage was calculated as the interquartile range of the bandpass diameter signal times $\sqrt{2}$ divided by the mean diameter. From the measurements of eight mice, we observed a mean pulsation percentage around 1% for the 0 μm deep plane and a mean pulsation percentage of 1.5% for the 100 μm deep plane (figure 2*c*).

To observe pulsation due to functional hyperaemia, we stimulated neural activity via whisker puffing [13]. We measured the dilation waveform induced by functional hyperaemia in both planes over the 90 s of the recording (figure 2*e*). Over the 30 s stimulation period (from 30 s to 60 s in figure 2*e*), we observed several dilation peaks. By dividing the peak diameter change by the mean diameter of the baseline (from 0 s to 30 s in figure 2*e*), we obtained a pulsation percentage of 6% for the 0 μm deep plane and 11% for the 100 μm deep plane (figure 2*f*). Our experiments thus demonstrate that functional hyperaemia induces larger dilation amplitudes in the deep cross section of the penetrating arteries compared to the surface cross section.

4. Results of the simulations

4.1. With the valve mechanism, cardiac pulsations drive a net cerebrospinal fluid influx

We modelled flow driven by cardiac pulsations, which have high frequency (2–6 Hz) but small amplitude (1% to 5%). We first tested the model using an essentially rigid endfoot wall with elasticity $E_{endft} = 10^6$ Pa, roughly an order of magnitude higher than measured for artery walls [34]. In the $k_1/k_0 = 1$ case, where wall permeability remains constant and no valve action occurs, the inflow and backflow rates for each cycle were the same, resulting in zero net flow (figure 3*a,b*). With $k_1/k_0 > 1$, however, we observed less backflow than inflow and hence a net flow.
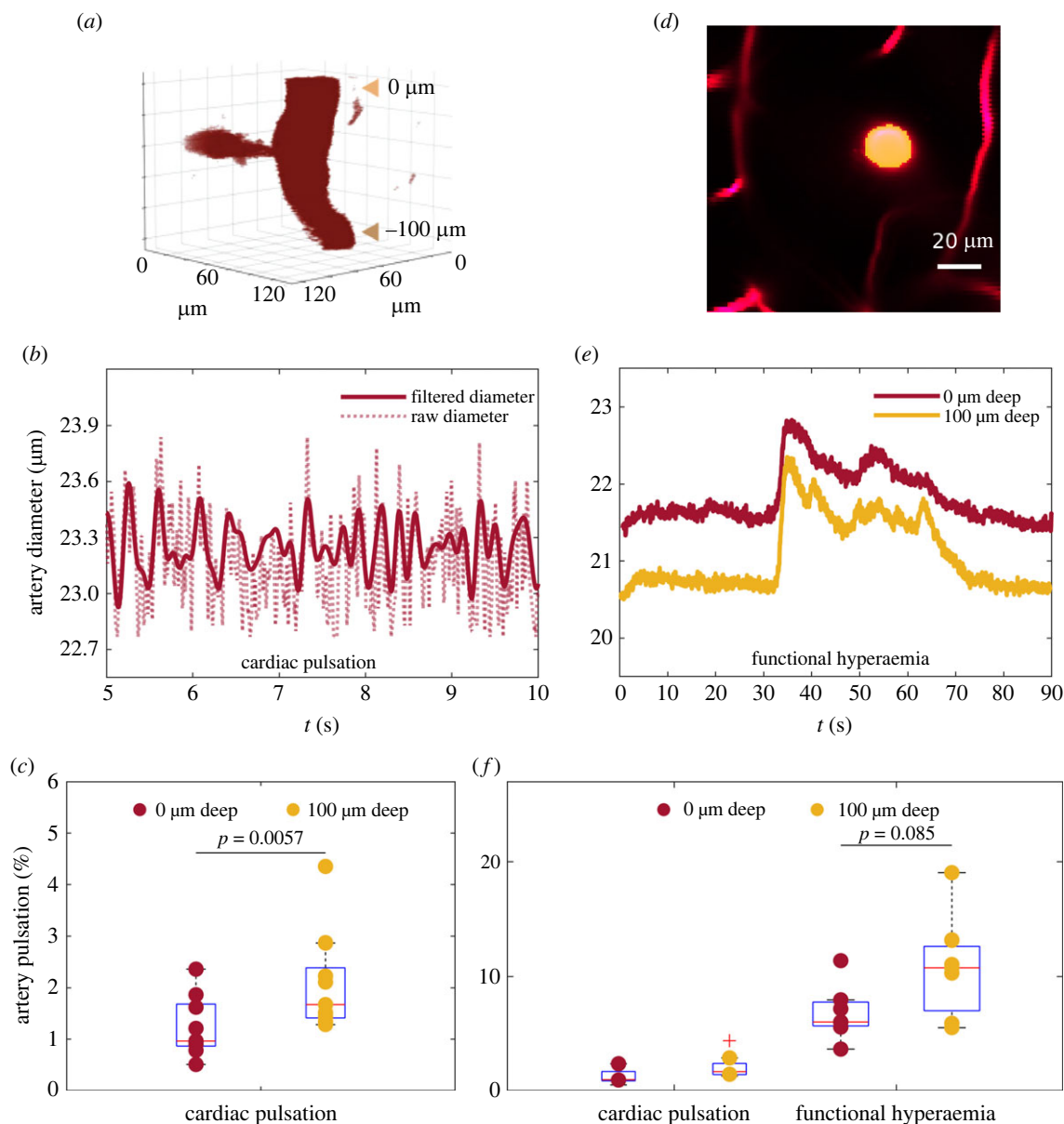
Figure 2. Measurements of cardiac pulsation and functional hyperaemia in the penetrating arteries. (a) A penetrating artery of a mouse, from depths 0 μm to 100 μm, as imaged *in vivo*. (b) Artery diameter variation, measured from area changes. (c) Average normalized artery diameter variation in the cardiac frequency band, at depths 0 μm and 100 μm, in $N = 8$ mice. Boxes show median and interquartile range. (d) Cross section of a penetrating artery of a mouse. The shaded yellow mask represents the result of the segmentation algorithm. (e) Artery diameter variation, measured from area changes during functional hyperaemia, averaged over $N = 7$ mice. (f) Average normalized artery diameter variation during cardiac pulsation, in $N = 8$ mice, and functional hyperaemia, at depths 0 μm and 100 μm, in $N = 7$ mice. Functional hyperaemia causes greater diameter variations than cardiac pulsation ($p < 10^{-4}$ for an unpaired t-test), and with both mechanisms, there is a trend toward greater diameter variation at greater depths.

For a more compliant endfoot wall, we expect increased wall deformation that would absorb more of the arterial pump energy. To test this expectation, we performed simulations varying E_{endft}. We measured the mean flow rate $\int_0^{t_0} q \, dt / t_0$ (where q is the instantaneous volume flow rate) and the pressure difference between the two ends of the PVS. Both increased with k_1/k_0 and decreased for a more compliant endfoot wall, as expected (figure 3c–e). We observed a mean pressure gradient at the pial entrance of the order of $100 \, \text{Pa} \, \text{m}^{-1}$ (figure 3f), which matches experimental measurements [35] and other numerical models [10,21].

4.2. The valve mechanism is suppressed during wakefulness

In vivo experiments show that, compared to sleep or anaesthesia, wakefulness results in smaller ECS permeability and reduced CSF influx [22,36]. In this section, we show that our model likewise predicts reduced net flux during wakefulness. We modelled the difference between sleep and wakefulness by varying k_{ecs} from $2 \times 10^{-17} \, \text{m}^2$ to $1 \times 10^{-16} \, \text{m}^2$. For small k_{ecs} (wakefulness), we found an increased pressure response in the ECS and a reduced net flow of CSF (figure 4a,b). Higher pressure in the ECS during wakefulness (figure 4c,d) hinders CSF entering across the endfoot wall, resulting in less axial CSF influx.

4.3. A lumped-parameter model and the frequency analysis

We further simplify our model in terms of lumped parameters (details of the simplified model are included in appendix B). There are two pathways by which fluid can
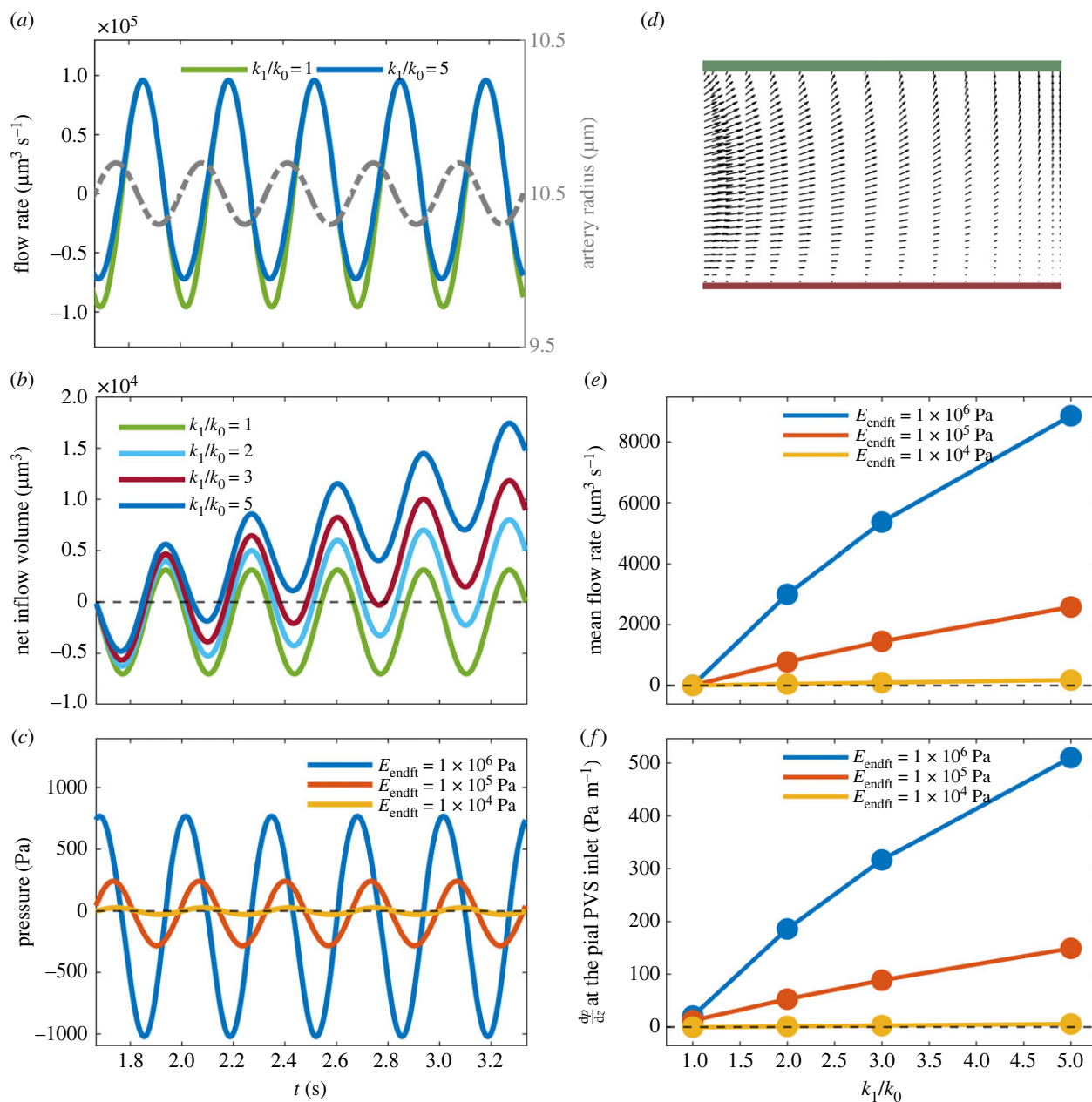
Figure 3. Flow and pressure driven by 10 cycles of cardiac pulsation ($f = 3$ Hz). (*a*) As the artery dilates and constricts, the volume flow rate at the inlet of the penetrating perivascular space oscillates symmetrically around zero if no valve mechanism is implemented ($k_1/k_0 = 1$), but favours inflow when the valve mechanism is active ($k_1/k_0 = 5$). (*b*) Net volume of fluid pumped into the penetrating perivascular space, starting at the beginning of the fifth cycle to avoid transients. The volume fluctuates but increases, on average, at a rate depending on the permeability ratio k_1/k_0. (*c*) Pressure fluctuations in the penetrating perivascular space, varying with endfoot wall elasticity E_{endft}. In all cases, $k_1/k_0 = 5$. Softer walls deform more, reducing pressure fluctuations. (*d*) Mean fluid velocity in the perivascular space, over the last five cardiac cycles, shows net inflow. (*e*) The mean flow rate at the inlet increases with permeability ratio and wall elasticity. (*f*) The mean pressure gradient at the pial perivascular space inlet (over five cycles) likewise increases with permeability ratio and wall elasticity.

enter or exit the penetrating PVS, as sketched in figure 5*a*: fluid can be exchanged with the pial PVS or the ECS, via the endfoot wall. R_{pial}, R_{ecs} and R_{endft} represent the flow resistance in the pial PVS, ECS and endfoot wall, respectively. Since the value of R_{endft} depends on the pressure difference (analogous to voltage) across it according to equation (2.1), we represent it as a Zener diode, a circuit device whose resistance is much higher (though not infinite) for reverse flow than forward flow. Flow through the capillary PVS is negligible because their resistance far exceeds that of the ECS and endfoot wall. The flow resistance within the penetrating PVS itself is negligible.

Fluid motion induced by the prescribed arterial pulsation is modelled as a flow source (analogous to a current source)

with a volume flow rate equal to the rate of change of the artery volume:

$$q_{\text{art}} = \frac{\partial}{\partial t}(\pi(r_1 + h)^2 l) \approx 2\pi r_1 l \frac{\partial h}{\partial t}. \tag{4.1}$$

Here, the final expression results from neglecting terms that are second-order small, given that $h \ll r_1$. In addition to the change of the artery volume, the pressure-dependent deformation of the endfoot wall (analogous to capacitance) also causes a change of PVS volume, which can be represented as a source with flow rate

$$q_{\text{compliance}} = \frac{\partial}{\partial t}(\pi l((r_1 + b + d)^2 - (r_1 + b)^2))$$

$$\approx 2\pi(r_1 + b)l \frac{\partial d}{\partial t} = C_{\text{endft}} \frac{\partial p}{\partial t}, \tag{4.2}$$
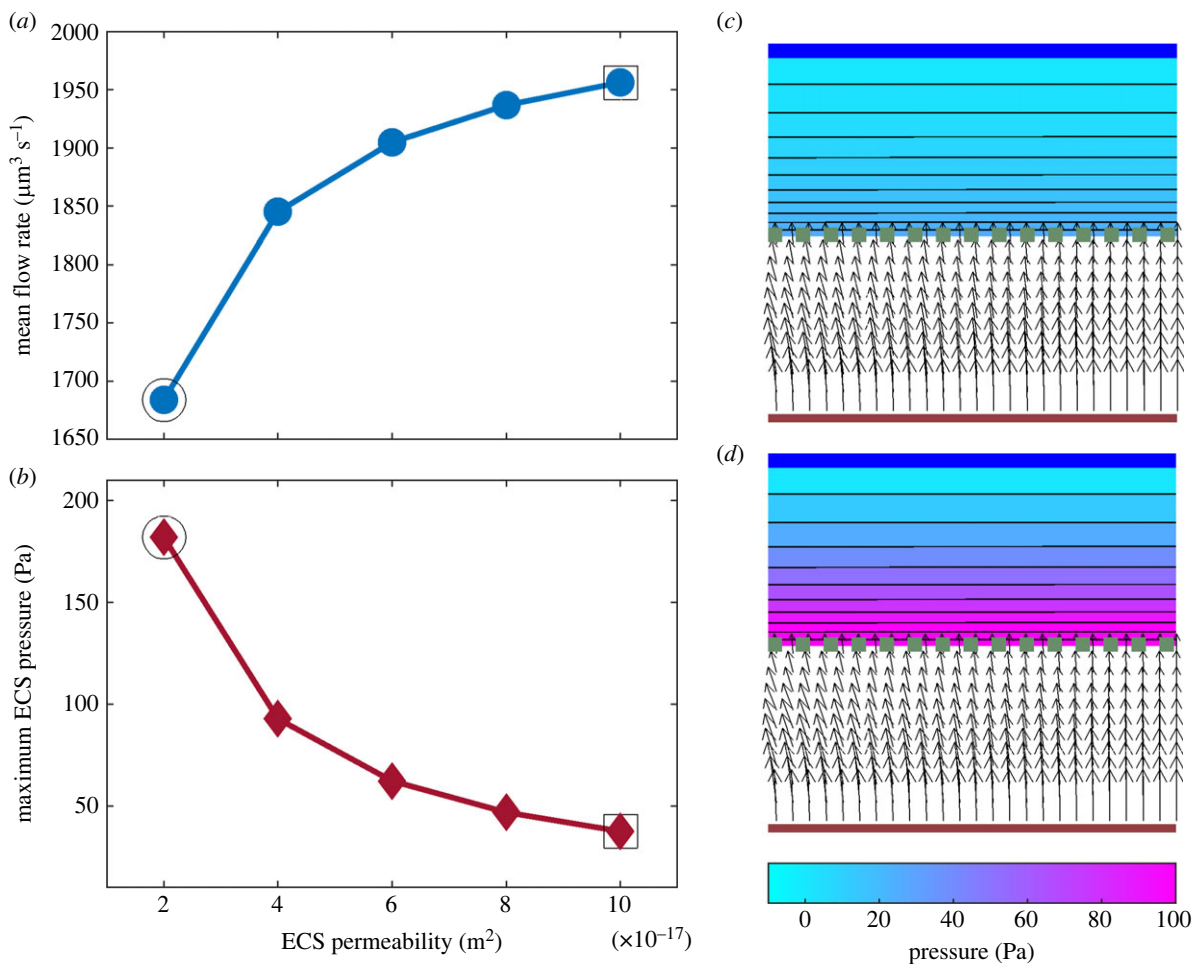
Figure 4. Modelling sleep–wake differences by varying the permeability of the extracellular space (ECS). (a) The mean flow rate at the pial entrance increases with ECS permeability. (b) The maximum pressure in the perivascular space decreases ECS permeability. (c) Instantaneous ECS pressure and PVS velocity, during artery dilation by 5%, with ECS permeability $k_{ecs} = 1 \times 10^{-16}$ m^2, corresponding to points marked with circles in (a,b). (d) Instantaneous ECS pressure and PVS velocity, during artery dilation by 5%, with ECS permeability $k_{ecs} = 2 \times 10^{-17}$ m^2, corresponding to points marked with squares in (a,b). Greater permeability, as expected during sleep, leads to much lower pressure gradients in the ECS, even for stronger artery dilation.

where $C_{endft} = 2\pi l(r_1 + b)^2 E_{endft}^{-1}$, given that the deformation of the endfoot wall is proportional to pressure (equation (B8) in appendix B). The system is then a parallel circuit (figure 5a) governed by

$$\frac{p}{R_{endft} + R_{ecs}} + \frac{p}{R_{pial}} + C_{endft}\frac{\partial p}{\partial t} = q_{art}. \quad (4.3)$$

For convenience, we define $q_{pial} = -pR_{pial}^{-1}$ (the inflow rate from the pial PVS) and $q_{ecs} = p(R_{endft} + R_{ecs})^{-1}$ (the outflow rate to the ECS).

Figure 5b shows that the value of q_{pial} predicted by the lumped-parameter model is close to that of the fluid dynamical model. Since the lumped-parameter model is simple, we can quickly study analytically how the system responds to arterial pulsations of different frequencies. Using equation (2.2) in the absence of the valve mechanism ($R_{endft} = 0$) and neglecting transients, we can solve for q_{pial} analytically:

$$q_{pial} = \frac{4\pi^2 r_1 l h_{cp} f}{R_{pial} C_{endft}\sqrt{4\pi^2 f^2 + \left(\frac{1}{R_{eff}C_{endft}}\right)^2}} e^{2\pi i(ft - (\arctan(2\pi f R_{eff} C_{endft})/2\pi))},$$

$$(4.4)$$

where R_{eff} is the effective flow resistance of the lumped-parameter model ($R_{eff}^{-1} = (R_{endft} + R_{ecs})^{-1} + R_{pial}^{-1}$). Though equation (4.4) does not account for the valve

mechanism, it fully describes how the arterial pulsation frequency f and the endfoot wall elasticity E_{endft} influence the flow rate.

The exponential term in equation (4.4) describes the phase of q_{pial}, from which we can calculate the phase difference between the arterial wall velocity and the inflow rate. In figure 5c, we calculate the phase difference for various pulsation frequencies f and E_{endft} and find that it matches the simulation result. Based on equation (4.4), the phase difference increases as we increase f or decrease E_{endft}, eventually converging to $-\pi/2$. The phase difference changes most rapidly when the pulsation timescale f^{-1} is similar to the characteristic relaxation time $R_{eff} C_{endft}$ of the compliant system.

The initial factor in equation (4.4) describes the maximum value of q_{pial} and the maximum value of p. In figure 5d, we plot the maximum value of p for various pulsation frequencies f and E_{endft}, which also matches the simulation result with the valve. When f is small or E_{endft} is large, the maximum value of p is proportional to f, whereas when f becomes large or E_{endft} becomes small, the maximum value of p approaches a constant. Both limiting cases are consistent with our expectations from the lumped-parameter model. First, equation (4.1) implies that $q_{art} \sim \partial h/\partial t \sim fh$. Then, when f is small, the compliance term in equation (4.3) becomes negligible, so that $p \sim q_{art} \sim f$. On the other hand, when f is large, the compliance term dominates because ∂
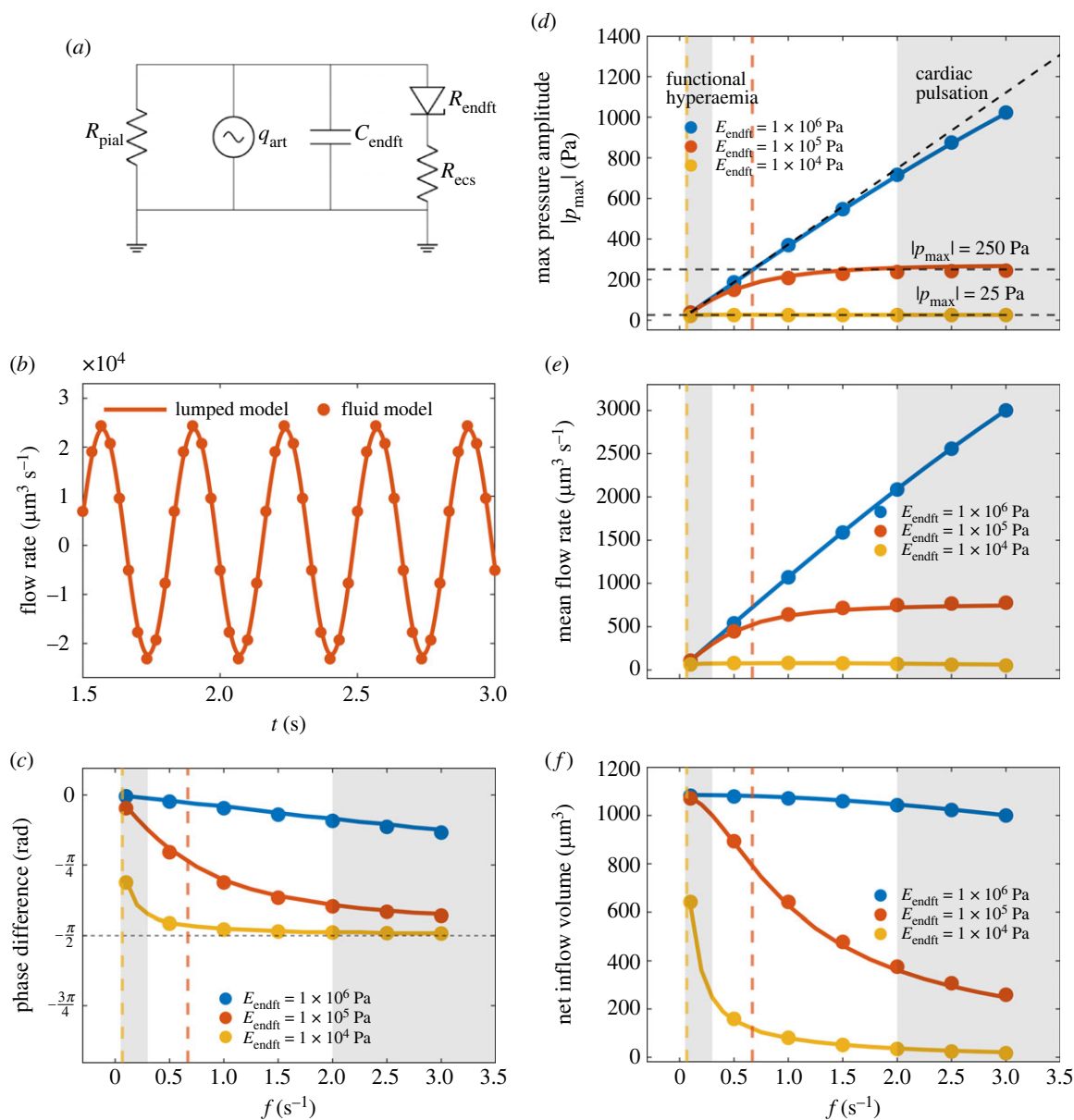
Figure 5. The lumped-parameter model simplified from the fluid dynamic model and the frequency analysis. (*a*) Sketch of the lumped-parameter model. The volume change due to arterial pulsation is modelled as a flow source. Pathways to the pial PVS and the ECS each have a hydraulic resistance, and the endfoot wall is compliant. (*b*) In the absence of valve action, the fluid dynamical and lumped-parameter models predict similar pial PVS inflow rates in response to cardiac pulsations. (*c*) In the absence of valve action, the two models predict similar phase difference between wall velocity and q_{pial}. In (*c*,*d*), simulation results are plotted as circles, and predictions from the lumped-parameter model are plotted as curves. In (*c–f*), vertical dashed lines mark the characteristic frequencies $(R_{eff}\, C_{endft})^{-1}$. (*d*) In the absence of valve action, the two models predict similar maximum pressure p_{max}, which is proportional to f when f is small and approaches a constant value when f is large. (*e*) With valve action, the lumped-parameter model (dots) and the fluid dynamical model (solid lines) predict that the mean flow rate varies with f in much the same way as p_{max} does in the absence of valve action. (*f*) With valve action, the lumped-parameter model (dots) and the fluid dynamical model (solid lines) predict that the net inflow per cycle is maximum at low frequencies and decreases rapidly as f exceeds $(R_{eff}\, C_{endft})^{-1}$.

$p/\partial t \sim f\, p$, so $p \sim q_{art}/f$, a constant. The small and large frequency ranges are separated by $(R_{eff}\, C_{endft})^{-1}$, the inverse of the characteristic relaxation time.

In figure 5*e*, we show the mean inflow rate per cycle with the valve mechanism in effect (with $k_1/k_0 = 2$), which follows the same trend as the maximum p in figure 5*d*, again increasing with f at low frequencies but saturating at high frequencies, with the two frequency regimes separated by $(R_{eff}\, C_{endft})^{-1}$. The increase with f at low frequencies can be explained by the higher wall velocities that occur at higher frequencies (for constant amplitude). Saturation at higher frequencies can be explained by rapid endfoot deformations damping the pumping. In the same way, as f increases, the net inflow volume per one cycle is nearly constant for large

E_{endft} but gradually decreases for small E_{endft}, still depending on $(R_{eff}\, C_{endft})^{-1}$ (figure 5*f*). The numerical solutions of the lumped-parameter model (solid line) and the full fluid dynamic model (dots) in figure 5*e*,*f* match very well.

4.4. With the valve mechanism, functional hyperaemia drives a net cerebrospinal fluid influx in addition to that produced by cardiac pulsation

Next, we model flow driven when functional hyperaemia, which has a longer time scale (5–20 s) but a larger oscillation amplitude (10–20%), occurs in addition to cardiac pulsation (figure 6*a*). We observe an increased net inflow volume
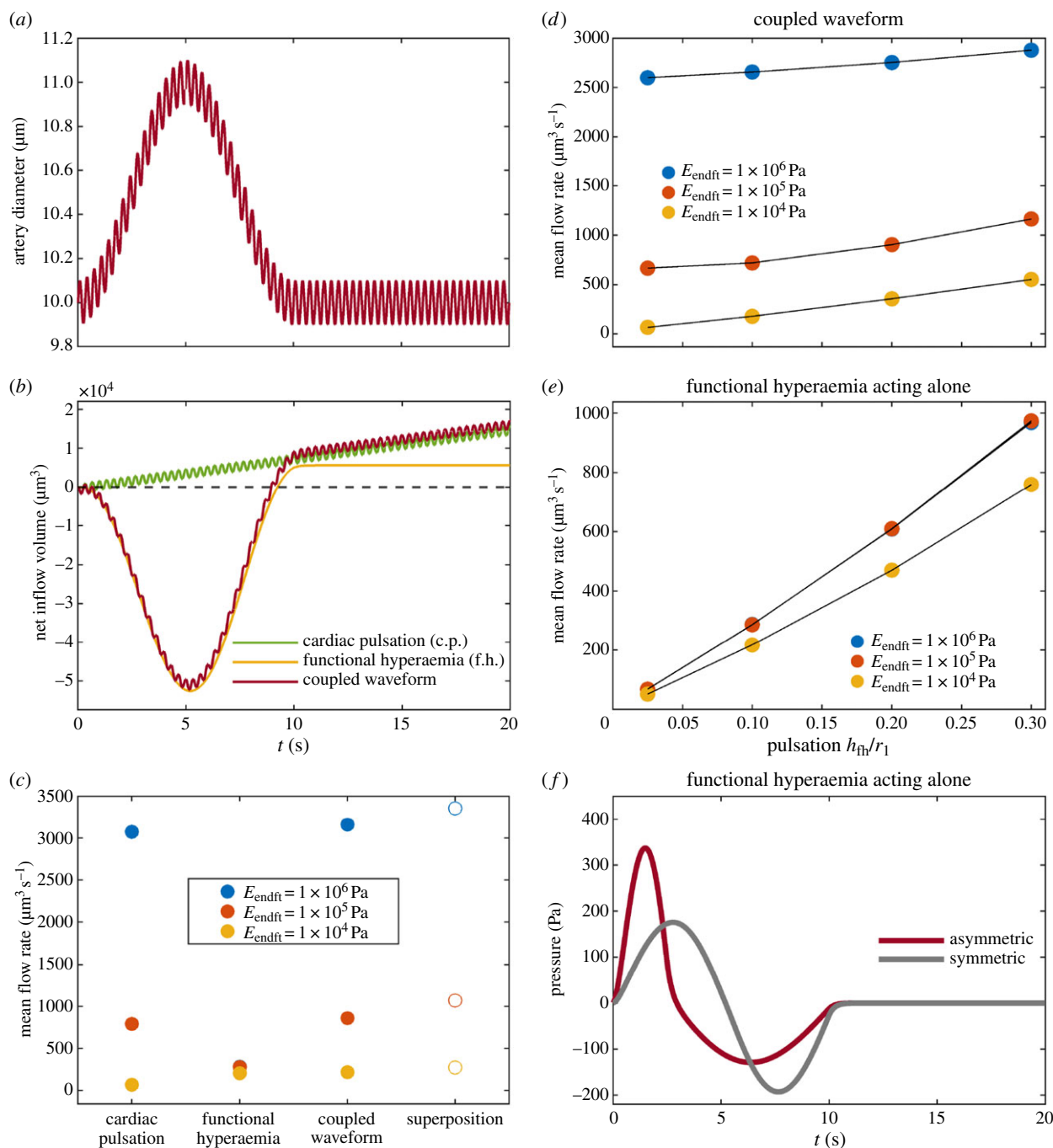
Figure 6. Modelling valve action during functional hyperaemia. (*a*) The arterial waveform that couples the cardiac pulsation and functional hyperaemia. (*b*) We observed an increased net inflow volume over time for the coupled waveform compared to cardiac pulsation or functional hyperaemia acting alone. (*c*) Comparison between the mean inflow rate driven by cardiac pulsation, functional hyperaemia, the coupled waveform and the superposition of the first two mean flow rates. (*d*) The mean flow rate driven by the coupled waveform increases as with the dilation percentage, h_{fh}/r_1, and the increase is more significant for $E_{endft} = 10^4$ Pa. (*e*) The mean flow rate driven by functional hyperaemia acting alone increases with h_{fh}/r_1. (*f*) Asymmetric variation includes a quick dilation that greatly increases pressure.

for the coupled waveform compared to that of cardiac pulsation acting alone (figures 1*d* and 6*b*). We can also consider the hypothetical situation, which is physiologically impossible but nonetheless informative, of functional hyperaemia acting in the absence of cardiac pulsation (figure 1*e*). We observe that acting alone, functional hyperaemia drives less net inflow than either cardiac pulsation alone or their combination (figure 6*b*).

In figure 6*c*, we show the mean inflow rates driven by cardiac pulsation alone, functional hyperaemia in combination with cardiac pulsation, and functional hyperaemia alone. Though the mean flow rate for the coupled waveform is larger than for either mechanism acting alone, it is also

smaller than the sum of the mean flow rates induced independently by the two mechanisms. Valve action is a nonlinear process, so superposition does not hold; the rectified, summed flow is smaller than the sum of the rectified flows (see appendix B).

We also observe that the mean flow rate driven by the cardiac pulsation is larger than the mean flow rate driven by functional hyperaemia for large E_{endft}, which is consistent with figure 5*e*. That is because there are many cycles of cardiac pulsation during one episode of functional hyperaemia (figure 6*a*). However, when the compliance of the endfoot wall is relatively low ($E_{endft} = 10^4$ Pa), functional hyperaemia drives a larger mean flow rate than cardiac pulsation because

the more compliant endfoot wall filters the high-frequency pulsation (figure 5d–f).

In figure 6d, we plot the mean flow rate for the coupled waveform. The mean flow rate increases as h_{fh} increases. When E_{endft} is large, the increase is less significant because the cardiac pulsation (the high frequency pulsation) dominates the pumping mechanism. By contrast, for smaller E_{endft}, functional hyperaemia dominates, and the increase of mean flow rate with h_{fh} is significant. In figure 6e, we plot the mean flow rate for the functional hyperaemia waveform acting alone. The mean flow rate increases as h_{fh} increases and is less affected by E_{endft} (the mean flow rate for $E_{endft} = 10^6$ Pa is nearly identical to that for $E_{endft} = 10^5$ Pa).

A previous study [12] found that a more realistic, asymmetric artery pulsation waveform, composed of a fast dilation and a slow constriction, increased the net flux across the endfoot wall, perhaps because fast dilation pushes more fluid into the ECS. We compared the effects of a simple pulsation waveform to those of the more realistic, asymmetric waveform (figure 1e) considered in [12]. Pressure in the PVS increased rapidly during fast dilation, reaching a large maximum value (figure 6f). During slow constriction, however, the reverse pressure amplitude change was weaker but slower. On the other hand, the simple pulsation waveform induced pressures of nearly equal amplitude during dilation and constriction. We also observed an 8% increase in the axial net flux for the more realistic, asymmetric waveform, when compared with the simple waveform, given $k_1/k_0 = 2$, $E_{endft} = 10^5$ Pa.

5. Discussion

Here, we propose the existence of valve-like action at the astrocyte endfeet as an explanation for the observed directed net flow in PVSs. Our simulations modelling that action as a pressure-dependent permeability predict that flow from PVS to ECS during artery dilation exceeds flow in the reverse direction during constriction, resulting in net fluid motion over time in the direction parallel to blood flow. The dilation amplitudes we impose are based on our new *in vivo* measurements. We find that greater variation of permeability with pressure leads to greater net flow. Greater rigidity of the surrounding brain tissue also increases net flow, along with instantaneous pressure fluctuations in the PVS. Reduced permeability of surrounding brain tissue, as expected during wakefulness, leads to reduced net flow and increased mean pressure in the ECS, consistent with prior observations that glymphatic function is reduced during wakefulness. Net flow is driven by artery wall motions with frequency and amplitude characteristic of cardiac pulsation or functional hyperaemia, although some frequencies pump more effectively than others (figure 6e), and by either symmetric or asymmetric pulsation waveforms.

Thus, the presence of valve-like action at the endfeet is consistent with many phenomena observed previously, including strong pumping by functional hyperaemia [11,13,21] and pumping by cardiac pulsations in the absence of functional hyperaemia [3–5]. Because our model assumes artery dilation and constriction to be uniform along the penetrating PVS, the observed effects do not depend on wavelength, wave speed, or the presence of travelling waves, in contrast to proposed peristalsis-like mechanisms

[6]. Nor do the observed effects require temporal asymmetry of the artery pulsation waveform, though rapid dilation does increase net flow, consistent with prior modelling [12]. In our simulations, that effect can be explained by the concomitantly higher instantaneous pressure, which coincides with increased permeability (and therefore lower resistance) at the endfoot wall. We also point out that flow rectification is a nonlinear phenomenon, and by definition, nonlinearity is amplified as magnitudes (of velocity and pressure, in this case) grow. That said, the presence of valve-like action does not exclude other proposed pumping mechanisms, such as impedance pumping [13,37].

The pumping mechanism proposed here is based on the assumption that k_{endft} is larger when $p > p_{ecs}$ than when $p \le p_{ecs}$ (equation (2.1)), which is supported by a recent study of the mechanics of the endfoot gaps [14]. One might, alternatively, imagine that k_{endft} or k_{ecs} is smaller when $p > p_{ecs}$, which would lead to a reverse flow (opposite the direction of blood flow) in our model. The gaps between end feet and poles in the ECS might conceivably shrink when being squeezed by the pressure difference, causing reduced permeability. However, given the consistent experimental observations of forward CSF flow, we adopt the former assumption for our pumping model.

The pressures predicted by our model depend sensitively on the elasticity of the endfoot wall and the elasticity and permeability of the surrounding tissue. In some cases, PVS pressure reached -1000 Pa $= -7.5$ mmHg (figure 3c). Though measurements of the pressure distribution in the brain *in vivo* are quite difficult, these values are much higher than the expected approximately 1 mmHg maximum pressure difference across the glymphatic system [27,38]. Those extreme pressures, however, occurred only when the wall elasticity was $E_{endft} = 10^6$ Pa, much stiffer than we would expect [21,35]. With a smaller elasticity ($E_{endft} = 10^5$ Pa), PVS pressure reaches 200 Pa $= 1.5$ mmHg, more reasonably. The pressure gradient at the PVS inlet was around 100 Pa m^{-1}. Recent work using artificial intelligence velocimetry [35] reports a time-averaged pressure gradient of 275 Pa m^{-1} in pial (not penetrating) PVS, which is of the same order of magnitude. Similar values were found in recent simulations [10,21]. In the ECS, maximum pressure ranged from about 50 Pa $= 0.38$ mmHg when the permeability was $k_{ecs} = 10^{-16}$ m^2 to 200 Pa $= 1.5$ mmHg with $k_{ecs} = 2 \times 10^{-17}$ m^2 (figure 4b).

An effective valve mechanism does not necessarily require discrete, localized valves: it can be produced by an asymmetry along the flow pathway. Candidates for valves may include the astrocyte endfeet and valves along the perivenous space or the lymph vessels (the exit of the CSF pathway). Besides valves, the volume change of the brain during sleep and the impedance pumping mechanism [37] may also contribute to that asymmetry.

One important model proposed that, because a functional hyperaemia cycle includes a rapid dilation and a slow constriction, it may push more CSF into the poroelastic ECS than it pulls back [21]. We consider a penetrating artery of length 1000 µm, a typical length for the mouse brain [25]. Owing to the small aspect ratio ε, solving the creeping flow equations numerically is more challenging than solving the thin-film equations [20]. More importantly, since p scales with $1/\varepsilon^2$ for creeping flow, a longer penetrating artery can drive a larger pressure change that pumps the flow.

In our model, a pressure difference between the periarterial space and the perivenous space is the driver for advective flow in the ECS [25], which is necessary for our valve mechanism. According to Darcy's Law, the flow speed in the ECS is proportional to the pressure difference $p_{artery} - p_{venule}$ and the permeability k_{ecs}, and inversely proportional to the distance b_{ecs} between the periarterial space and the perivenous space. While the distance is constant, and the arterial pump determines the pressure difference, the ECS permeability varies from sleep to wake. From sleep to wakefulness, the porosity of the brain decreases from 0.234 to 0.141, while the tortuosity increases only very slightly, from 1.176 to 1.196. From these values, we estimate an approximately 4.82 times greater ECS permeability during sleep than during wakefulness based on the Kozeny–Carman equation [22,39]. The lower ECS permeability during wakefulness creates higher flow resistance, suppressing the entire glymphatic circulation. The ECS is treated as a homogeneous medium in our model. We could incorporate spatial-dependent porosity, toruosity and permeability, which would be valuable in future modelling to incorporate the inhomogeneities in the ECS [40]. The mechanical properties of the endfeet might also vary between sleep and wakefulness, potentially influencing our model. Future experimental measurements are needed to address this aspect.

The flow rates predicted by our model are broadly consistent with prior values obtained from experiments and simulations. In the cardiac pulsation simulation, we find a mean volume flow rate of order $1000 \, \mu m^3 \, s^{-1}$ (for $k_1/k_0 = 2$, $E_{endft} = 1 \times 10^5$ Pa, figure 3e). A mouse has around 320 penetrating arteries branching from the MCA [41], from which we can estimate a total volume flow rate of $320 \times 1000 \, \mu m^3 \, s^{-1} = 3.2 \times 10^5 \, \mu m^3 \, s^{-1}$ in the PVS of an MCA. An experimental measurement reported a volume flow rate of $\sim 4.5 \times 10^4 \, \mu m^3 \, s^{-1}$ for an MCA [15,35]. Our simulation thus gives a fairly close prediction, given that some key parameters, such as E_{endft}, k_{endft}, k_1/k_0 and k_{ecs}, have large uncertainty. Various experimental studies indicate that the elastic modulus of the endfeet, E_{endft}, lies in the range 10^2–10^4 Pa [34,42–44]. For the softest endfoot wall, the pressure difference across the wall is limited to small values that would not admit any significant through flow with the assumed values of the permeability k_{endft} [20].

The astroglial aquaporin-4 water channels (AQP4) in the endfeet allow faster fluid transport: AQP4 knock-out mice have lower CSF influx [45]. This might be due to an effect of AQP4 on the properties of the endfoot wall. Thus, the range of values of k_{endft} might change, compared to previous estimations, if the role of AQP4 is considered [28]. It has been suggested that AQP4 might affect the stiffness and flexibility of the endfoot wall [14].

The lumped-parameter model reveals what determines the portion of cardiac pulsation and functional hyperaemia in pumping the CSF inflow. While the former is 50 times more rapid, the latter is five times larger in amplitude. Both factors can contribute to a higher inflow rate (figures 5e and 6e,f). The model points out that deformation of the endfoot wall plays a role as a lowpass filter (the compliance) that limits the pumping efficiency of the cardiac pulsation (figure 5e,f). In the simulations, for $E_{endft} > 10^4$ Pa, cardiac pulsation dominates the inflow (figure 6b,c,d), but functional hyperaemia gradually becomes a comparable driver as E_{endft} decreases (figure 6c). The numerical solutions of the lumped-parameter model and the fluid-dynamic model match each other very well (figure 5e,f). While the fluid-dynamic model resolves the flow spatially, the lumped-parameter model represents a pure time-varying system without spatial resolution and is therefore computationally inexpensive and quite suitable for vascular network modelling [27].

Another important observation is that although coupling functional hyperaemia and cardiac pulsation drives more flow than either mechanism acting alone, it drives less than the superposition of them pumping independently (figure 6c). That said, the coupled waveform is more realistic, as functional hyperaemia never occurs in the absence of cardiac pulsation. On the other hand, while functional hyperaemia happens only occasionally, cardiac pulsation, CSF inflow is consistently observed as a continual process in experiments [3,5,13,35,46]. The fact that cardiac pulsation is approximately 30 times more rapid than functional hyperaemia, and occurs all the time, makes it a much stronger driver of CSF flow (figure 6b–d), at least in the context of our model.

For given values of k_{ecs} and b_{ecs}, the flow speed is determined by the pressure gradient driven by the arterial motion. The cardiac pulsation amplitude for a pial artery is usually about 1% of the artery diameter and 0.5% of the PVS width [16]. For penetrating arteries, a time-averaged pressure difference of 10 Pa over an axial distance of 1000 μm can drive a $1 \, \mu m \, s^{-1}$ net interstitial flow in the ECS. Because flow measurements in the ECS are exceptionally challenging, it has long been debated whether there is any significant flow there. A recent theoretical analysis [39] demonstrates that the permeability increase from wake to sleep reduces diffusive transport slightly but would increase advection significantly (due to reduced hydraulic resistance), suggesting that a flow in the ECS might help explain the observed increase in brain clearance from wakefulness to sleep. Our valve model shows that a flow in the ECS might also be an important part of the mechanism that produces the net flow in the system of PVSs.

It is also important to point out that when there is an influx from the PVS to the ECS there must be a nearly simultaneous efflux somewhere, because the volume of the brain is nearly constant, and the fluid inside (CSF, interstitial fluid) is incompressible. The poroelasticity of the brain might allow a slight time lag between the influx and efflux, but they have to happen on the same time scale.

The predictions of our model are subject to additional caveats. First, we have modelled penetrating PVSs as open spaces, where flow is governed by the Navier–Stokes equation, but they may contain enough tissue that they should be modelled as a porous medium, with flow governed instead by the Darcy equation. Recent imaging of penetrating PVSs suggests this may be the case [47], although pial PVSs are known to be open [26]. In fact, whether penetrating PVSs are porous and what their permeability might be has been identified as the source of greatest uncertainty for brain-wide modelling of glymphatic flows [29]. That said, other modelling suggests a useful constraint: good perfusion throughout the brain seems to require that the resistance of penetrating PVSs (which is proportional to their permeability) be much greater than that of pial PVSs but much less than that of the ECS [27]. Regardless of the permeability of penetrating PVSs, valve action of the sort we suggest here would rectify oscillations and produce a net flow. Whether

the potential poroelasticity of the PVSs plays a role in the valve mechanism will be addressed in further studies.

Second, we have modelled the penetrating PVS as a circular annulus, concentric with the artery, but *in vivo* measurements show that large eccentricity is common, with the artery positioned against one wall of the PVS [48]. We expect that accounting for this eccentricity would lead to slightly different predictions. For an open PVS, eccentricity reduces the hydraulic resistance, tending to increase flow and reduce axial pressure gradients. On the side of the artery where the PVS is narrowest, dilation and constriction would cause larger local pressure fluctuations [8,49] and presumably stronger valve action. On the other side of the artery, however, pressure fluctuations would be smaller and valve action weaker. Future simulations might incorporate eccentric PVSs to explore the effect of these adjustments. A penetrating artery, along with its PVS, branches into smaller arterioles and smaller PVSs as it goes deeper into the brain tissue. These smaller PVSs likely will not contribute significant pumping because of their high hydraulic resistance, but they are still of interest for future brain-scale vascular network modelling. Previous work [27] incorporates the hydraulic resistance of PVSs all along the vascular network in a lumped-parameter model. Our local lumped-parameter model can be extended to a full vascular network model in a similar way, but with the proposed pumping mechanism included. This approach could also be applied to flow in the lymphatic vessel network, which is driven by artery wall motion and rectified by valves.

Third, we have not considered PVSs around veins in any detail, although they have been proposed as a route for fluid to leave brain tissue [50]. If fluid is passing from a higher-pressure ECS to a lower-pressure perivenous space, by the same reasoning discussed above, we would expect the endfoot wall to be compressed, shrinking gaps between endfeet and hindering flow. That is, we would naively expect valve action at the endfoot wall of a perivenous space to promote net flow in the direction opposite to that which has been observed *in vivo*. The valve mechanism proposed by Bork *et al.* [14], if acting at perivenous spaces, would also promote flow in the opposite direction, unless the wedge-shaped edges of endfeet were reversed. However, pulsatility, pressure, and its gradients are much lower in veins [1], so both sorts of valve action may be negligible there. Generally, far less is known about glymphatic efflux than about influx, making it a worthy topic for future studies.

Appendix A. Experimental protocol

Our animal experiments were approved by the Danish Animal Experiments Inspectorate or the University Committee on Animal Resources of the University of Rochester and were performed according to guidelines from the National Institutes of Health (NIH). The mice had ad libitum food and water access in an environment with a 12 h light/12 h dark cycle (lights on at 7.00). We used a mixture of males and females for the studies and, if not otherwise stated, we used C57BL/6JRj (Janvier). The mice were 11–15 weeks old.

The mice were anaesthetized with a ketamine/xylazine mixture (100 mg kg^{-1}; 10 mg kg^{-1}, i.p.) and fixed in a stereotaxic frame. Lidocaine (2 mg kg^{-1}, s.c.) and buprenorphine (0.05 mg kg^{-1}, i.p.) were injected for pain management. During surgery, the mice were positioned on a heating pad to maintain body temperature at 37°C. During surgery and subsequent imaging, anaesthesia was maintained by alternating between ketamine (50 mg kg^{-1}, s.c.) and ketamine/xylazine (50 mg kg^{-1}; 5 mg kg^{-1}, s.c.) injections every 30–45 min. Head fixing was required for imaging. The skin and fascia were cut away to expose the skull and dried with a cotton swab. A headplate was fastened with dental cement.

Whiskers were stimulated unilaterally by air puffs from a pneumatic pressure pump (Picospritzer, Parker) controlled by a digitizer (Molecular Devices, Axon Digidata 1550B plus HumSilencer), which was programmed via Clampex software (Axon pCLAMP). The whisker stimulations were delivered for 30 s, with 60 s interval (30 s of relaxation before the stimulation and 30 s of relaxation after each stimulation), and for protocol optimization, we applied frequencies of 5 Hz and pulse lengths of 10 ms. Air pressure was set to 20 psi. For each mouse, we performed several stimulations and computed a phase-averaged dilation waveform. Those stimulations with poor image quality, or stimulations that failed to generate neurovascular responses, were excluded.

Appendix B. Mathematical details of the models

B.1. The lubrication-theory model

B.1.1. The perivascular space domain

The PVS is an open space, and the flow there, assumed to be axisymmetric, obeys the Navier–Stokes equations and continuity equation in cylindrical coordinates (r, z):

$$\frac{\partial u}{\partial t} + u\frac{\partial u}{\partial r} + w\frac{\partial u}{\partial z} = -\frac{1}{\rho}\frac{\partial p}{\partial r} + \frac{\mu}{\rho}\left(\frac{1}{r}\frac{\partial u}{\partial r} + \frac{\partial^2 u}{\partial r^2} + \frac{\partial^2 u}{\partial z^2}\right), \quad \text{(B 1)}$$

$$\frac{\partial w}{\partial t} + u\frac{\partial w}{\partial r} + w\frac{\partial w}{\partial z} = -\frac{1}{\rho}\frac{\partial p}{\partial z} + \frac{\mu}{\rho}\left(\frac{1}{r}\frac{\partial w}{\partial r} + \frac{\partial^2 w}{\partial r^2} + \frac{\partial^2 w}{\partial z^2}\right) \quad \text{(B 2)}$$

and $\frac{1}{r}\frac{\partial(ru)}{\partial r} + \frac{\partial w}{\partial z} = 0,$ \hfill (B 3)

where $\mathbf{u} = (u, w)$ is the velocity field in cylindrical coordinates, p is the pressure, t is time, ρ is the density of the fluid and μ is the dynamic viscosity. These equations are subject to the following boundary conditions:

$$z = 0: \; q_{pvs} = q_{pial}, \;\; q_{pial} = k_{pial}(p_{pial} - p), \;\; p_{pial} = 0, \quad \text{(B4)}$$

$$z = l: \; q_{pvs} = q_{cap}, \;\; q_{cap} = k_{cap}(p - p_{cap}), \;\; p_{cap} = 0, \quad \text{(B5)}$$

$$r = r_1 + h: \; \mathbf{u} \cdot \mathbf{n} = 0, \;\; \mathbf{u} \cdot \mathbf{t} = 0 \quad \text{(B6)}$$

$$\text{and} \quad r = r_1 + b + d: \; \mathbf{u} \cdot \mathbf{n} = \frac{\partial d}{\partial t} + k_{endft}(p - p_{ecs}), \;\; \mathbf{u} \cdot \mathbf{t} = 0, \quad \text{(B7)}$$

where

$$d = (r_1 + b)\frac{p - p_{ecs}}{E_{endft}} \quad \text{(B8)}$$

is the deformation of the PVS outer wall (measured from $d_0 = r_1 + b$). Here, r_1 is the radius of the artery at rest, b is the width of the PVS, l is the length of the penetrating artery, h is the amplitude of artery pulsation, E_{endft} is the Young's modulus of the PVS outer boundary, q_{pvs} is the flow rate at the end of the penetrating artery PVS, q_{pial} is the flow rate in the pial PVS, q_{cap} is the flow rate in the precapillary PVS, k_{pial} and k_{cap} are the conductivities of the pial and precapillary inlet and outlet, and finally, p_{pial} and p_{cap} are the pressure in the pial and precapillary PVS (set to zero). The unit vectors normal and tangential to the artery wall are $\mathbf{n} = (0, 1)$ and $\mathbf{t} = (1, 0)$, respectively. We have used the lubrication approximation [20].

At the upstream pial PVS and the downstream precapillary PVS, we set a hydraulic resistance boundary condition to model the inflow and outflow (equations (B4) and (B5)), assuming a conserved flow rate across each interface. At the artery wall, we set non-slip and non-permeable boundary conditions (equation (B6)). The outer boundary of the PVS, formed by the astrocyte endfeet, is modelled as a thin, deformable, elastic layer of permeable but non-slip tissue (equation (B7)). A linear elastic law is used to relate the deformation of this boundary to the pressure difference across it [20].

The artery motion of cardiac pulsation is modelled by equation (2.2). The artery motion of functional hyperaemia is modelled by equation (2.3), where h_0 is the amplitude and f is the frequency. This waveform ensures that h and dh/dt are continuous (figure 1e).

At the valve-like PVS outer boundary, formed by astrocyte endfeet, the permeability k_{endft} is modelled by equation (2.1). During artery dilation, the increased pressure in the PVS opens the valve, allowing fluid to enter the ECS (figure 1b). During artery constriction, the valve closes and CSF motion is confined to the PVS (figure 1c).

To put the equations in non-dimensional form, we use the scalings

$$r = bR, \quad z = lZ, \quad t = \frac{T}{f}, \quad u = bfU, \quad w = lfW \quad \text{and}$$

$$p = \frac{\mu f}{\varepsilon^2} P, \quad \text{(B9)}$$

where each uppercase symbol signifies a dimensionless version of the corresponding lowercase symbol. Applying the

lubrication theory, we obtain the following equations:

$$\frac{\partial P_0}{\partial T} + A_0 \frac{\partial^2 P_0}{\partial Z^2} + A_1 \frac{\partial P_0}{\partial Z} + A_2 P_0$$
$$= \left[\frac{E(R_1 + H)}{R_1 + 1 + D_0}\right]\frac{\partial H}{\partial T} + A_2 P_{ECS} + \frac{\partial P_{ECS}}{\partial T}, \quad \text{(B10)}$$

$$W_0 = \frac{R^2}{4}\frac{\partial P_0}{\partial Z} + C_1 \ln(R) + C_2 \quad \text{(B11)}$$

$$\text{and} \quad U_0 = \frac{C_3}{R} - \frac{R^3}{16}\frac{\partial^2 P_0}{\partial Z^2} - \frac{R}{4}[2\ln(R) - 1]\frac{\partial C_1}{\partial Z} - \frac{R}{2}\frac{\partial C_2}{\partial Z}, \quad \text{(B12)}$$

where P_0, W_0 and U_0 are the leading order terms of P, W and U, respectively. A_0, A_1, A_2, C_1, C_2 and C_3 are known functions of Z and T. These equations are solved numerically using the Chebyshev spectral method [20].

Integrating the axial velocity (equation (B11)) over the cross section of the annulus, we obtain an expression for the volume flow rate:

$$Q_0(Z, T) = \int_0^{2\pi}\int_{R_1+H}^{1+R_1+D} W_0 R \, dR \, d\theta$$
$$= 2\pi\left[\frac{R^4}{16}\frac{\partial P_0}{\partial Z} + C_1\left(\frac{R^2\ln(R)}{2} - \frac{R^2}{4}\right) + \frac{C_2 R^2}{2}\right]\Bigg|_{R=R_1+H}^{R=1+R_1+D}. \quad \text{(B13)}$$

We model a hydraulic resistance at the PVS of the pial boundary, with a conserved flow rate across the interface:

$$Z = 0: \; Q_0(0, T) = Q_{pial},$$
$$Q_{pial} = K_{pial}(0 - P_0(0, T)). \quad \text{(B14)}$$

In the same way, we model a hydraulic resistance at the PVS of the capillary site:

$$Z = 1: \; Q_0(1, T) = Q_{cap}, \quad Q_{cap} = K_{cap}(P_0(1, T) - 0). \quad \text{(B15)}$$

At the artery site, we have

$$R = R_1 + H: \; \mathbf{U} \cdot \mathbf{n} = \frac{\partial H}{\partial T}, \quad \mathbf{U} \cdot \mathbf{t} = 0, \quad \text{(B16)}$$

where H is the amplitude of artery pulsation. At the PVS outer boundary, we have

$$R = R_1 + 1 + D: \; \mathbf{U} \cdot \mathbf{n}$$
$$= \frac{\partial D}{\partial T} + K_{endft}(P_0(Z, T) - P_{ECS}), \quad \mathbf{U} \cdot \mathbf{t} = 0, \quad \text{(B17)}$$

where

$$D = \frac{P_0(Z, T) - P_{ECS}}{E} \quad \text{(B18)}$$

is the (dimensionless) displacement of the PVS outer boundary, $K_{endft} = k_{endft}\mu(b\varepsilon^2)^{-1}$ and $E = E_{endft}\varepsilon^2(\mu f(R_1 + 1))^{-1}$.

B.1.2. The extracellular space domain
The ECS is modelled as an incompressible porous medium, with incompressible flow governed by Darcy's Law. The governing equations are

$$\mathbf{u}_{ecs}^* = -\frac{k_{ecs}}{\mu}\nabla p_{ecs} \quad \text{and} \quad \mathbf{u}_{ecs}^* = \mathbf{u}_{ecs} - \frac{\partial \mathbf{d}_{ecs}}{\partial t}, \quad \text{(B19)}$$

and

$$\nabla \cdot \left(\phi\mathbf{u}_{ecs} + (1 - \phi)\frac{\partial \mathbf{d}_{ecs}}{\partial t}\right) = 0 \quad \text{and} \quad \nabla \cdot \mathbf{d}_{ecs} = 0, \quad \text{(B20)}$$

Table 2. Dimensionless parameters.

U	axial CSF velocity	$U = u/bf$
W	radial CSF velocity	$W = \varepsilon w/bf$
R	radial coordinate	$R = r/b$
Z	axial coordinate	$Z = \varepsilon(z/b)$
T	time	$T = f\,t$
R_{ECS}	axial coordinate for the ECS	$R_{ECS} = r/b_{ecs}$
P	pressure in the PVS	$P = p\varepsilon^2/\mu f$
Re	Reynolds number	$Re = \varepsilon\rho fb^2/\mu$
Q	axial flow rate	$Q = q/b^2 lf = \varepsilon(q/b^3 f)$
R_1	artery diameter	$R_1 = r_1/b$
D	displacement of the PVS outer boundary	$D = d/b$
A_{PVS}	PVS cross-section area	$A_{PVS} = a_{pvs}/b^2$
ε	aspect ratio of the PVS	$\varepsilon = b/l$
H	artery dilation amplitude	$H = h/b$
E	elasticity of the PVS outer boundary	$E = E_{endft}\varepsilon^2/\mu f(R_1 + 1)$
K_{endft}	permeability of the PVS outer boundary	$K_{endft} = \mu k_{endft}/b\varepsilon^2$
K_{pial}	conductivity of the pial PVS inlet	$K_{pial} = k_{pial}/(b^2(b/\varepsilon f)) \cdot (\mu f/\varepsilon^2)$
K_{cap}	conductivity of the capillary PVS outlet	$K_{cap} = k_{cap}/(b^2(b/\varepsilon)f) \cdot (\mu f/\varepsilon^2)$
K_{recs}	permeability of the ECS	$K_{recs} = k_{ecs}/b_{ecs}^2\varepsilon^2$
K_{zecs}	permeability of the ECS	$K_{zecs} = k_{ecs}/l^2\varepsilon^2$
P_{ecs}	pressure in the ECS	$P_{ecs} = p_{ecs}\varepsilon^2/\mu f$
U_{ecs}	radial velocity in the ECS	$U_{ecs} = u_{ecs}/b_{ecs}f$
W_{ecs}	radial velocity in the ECS	$W_{ecs} = w_{ecs}/lf$
U_{ecs}	radial velocity in the ECS	$U_{ecs} = u_{ecs}/b_{ecs}f$
U^*	radial velocity relative to the endfoot wall motion	$U^* = (u - \partial d/\partial t)/bf$
W_{ecs}^*	radial velocity in the ECS relative to the solid phase motion	
U_{ecs}^*	radial velocity in the ECS relative to the solid phase motion	

where $\mathbf{u}_{ecs} = (u_{ecs}, w_{ecs})$ is the velocity of the fluid phase in the ECS, ϕ is the porosity, $\mathbf{d}_{ecs}$ is the deformation of the solid phase in the ECS, $\mathbf{u}_{ecs}^*$ is the velocity field relative to the solid phase velocity, and p is the pressure inside the ECS. The dynamic viscosity μ of the CSF and the permeability k_{ecs} of the ECS are both assumed to be uniform. Applying all four of the above equations, we have

$$\nabla^2 p_{ecs} = 0. \quad (B\,21)$$

Across the PVS outer boundary, CSF enters or leaves the ECS from the PVS, and the velocity must be continuous there:

$$r = r_1 + b: \ u_{ecs}^* = u^*, \quad (B\,22)$$

where $u^* = k_{endft}(p - p_{ecs})$ is the velocity across the PVS endfoot wall measured relative to the deformation velocity of the endfoot wall.

For the boundary at the outer radius of the ECS, corresponding to efflux at the nearest venule, we assume free surfaces and require

$$r = r_1 + b + b_{ecs}: \ p = 0. \quad (B\,23)$$

For the boundaries at the two ends, we assume zero axial

pressure gradient:

$$z = 0 \quad \text{and} \quad z = 1: \ \frac{\partial p_{ecs}}{\partial z} = 0. \quad (B\,24)$$

Since the deformation of the endfeet is only in the r direction and the venule site is a free surface, if we also assume negligible displacement in the z-direction, we obtain the analytical solution

$$\mathbf{d}_{ecs}(r, z, t) = \left[d(z, t)\left(\frac{r_1 + b}{r}\right), 0\right]. \quad (B\,25)$$

To put the equations in dimensionless form, we use the scalings

$$r_{ecs} = b_{ecs}R_{ecs}, \quad u_{ecs}^* = b_{ecs}fU_{ecs}^*, \quad w_{ecs}^* = lfW_{ecs}^*$$
$$\text{and} \quad p_{ecs} = \frac{\mu f}{\varepsilon^2}P_{ecs}. \quad (B\,26)$$

The equations in dimensionless form are then

$$U_{ecs}^* = -K_{recs}\frac{\partial P_{ecs}}{\partial R_{ecs}}, \quad (B\,27)$$

$$W_{ecs}^* = -K_{zecs}\frac{\partial P_{ecs}}{\partial Z} \quad (B\,28)$$

and $\quad K_{recs}\left(\dfrac{1}{R}\dfrac{\partial P_{ecs}}{\partial R}+\dfrac{\partial^2 P_{ecs}}{\partial R_{ecs}^2}\right)+\dfrac{b_{ecs}}{l_0}K_{zecs}\dfrac{\partial^2 P_{ecs}}{\partial Z^2}=0,$ (B 29)

where $K_{recs}=k_{ecs}(b_{ecs}^2\varepsilon^2)^{-1}$ and $K_{zecs}=k_{ecs}(l_0^2\varepsilon^2)^{-1}$, and the boundary conditions in dimensionless form are

$$R_{ecs}=\frac{r_1+b}{b_{ecs}}: U_{ecs}^*=\frac{b}{b_{ecs}}U^*,$$ (B 30)

$$R_{ecs}=\frac{r_1+b+b_{ecs}}{b_{ecs}}: P_{ecs}=0$$ (B 31)

and $\qquad Z=0,\quad Z=1:\dfrac{\partial P_{ecs}}{\partial Z}=0.$ (B 32)

The flow in the ECS domain is computed using a custom-developed Poisson equation solver. For the lubrication-theory model, the dimensional parameters are listed in table 1, and the dimensionless parameters are listed in table 2.

B.2. The lumped-parameter model

B.2.1. Lumped parameters

We further simplify our model in terms of lumped parameters. All coefficients in equation (4.3) can be identified from the coefficients in the fluid dynamical equation (B 10), neglecting some higher-order infinitesimal terms. Here, we present another way to derive the coefficients through direct analysis of the pressure–flowrate lumped-parameter model (equation (4.3)).

Fluid motion induced by the prescribed arterial pulsation is modelled as a flow rate source (analogous to the current source in figure 5a) with a volume flow rate equal to the rate of change of the artery volume, described by equation (4.1).

There are three pathways by which fluid can enter or exit the penetrating PVS, as sketched in figure 5a. Fluid can be exchanged with the pial PVS or the ECS, via the endfoot wall. Due to high resistance, flow through the capillary PVS is negligible. Each pathway has a hydraulic resistance, and ultimately connects to a place where the pressure (analogous to voltage) is zero. By calculation, the resistance of the pial pathway is $R_{pial}=k_{pial}^{-1}=1.06\times 10^{16}\,\mathrm{kg\,m^{-4}\,s^{-1}}$.

Though the resistance of the endfoot wall and that of the ECS depend on the surface area change of the endfoot wall (due to the deformation), they are small terms and we neglect them here for simplicity. Therefore, the resistance of the endfoot wall is inversely proportional to its area and its area-normalized permeability k_{endft}, which is pressure-dependent:

$$R_{endft}=\frac{1}{2\pi l(r_1+b)k_{endft}}$$
$$=\begin{cases}4.0\times 10^{16}\,\mathrm{kg\,m^{-4}\,s^{-1}} & p>p_{ecs}\\ 8.0\times 10^{16}\,\mathrm{kg\,m^{-4}\,s^{-1}} & p\leq p_{ecs},\end{cases}$$ (B 33)

for $k_1/k_0=2$. We only consider the resistance of the ECS R_{ecs} in the radial direction, which is

$$R_{ecs}=\frac{\mu}{2\pi lk_{ecs}}\ln\frac{r_1+b+b_{ecs}}{r_1+b}=2.56\times 10^{15}\,\mathrm{kg\,m^{-4}\,s^{-1}}$$ (B 34)

for $k_{ecs}=10^{-16}\,\mathrm{m^2}$. The logarithmic term in equation (B 33) is derived from equation (B 20) in the annular ECS domain [25,30].

The deformation of the endfoot wall can be modelled as the capacitance in the circuit, described by equation (4.2),

with a value $C_{endft}=(2.51\times 10^{-12}\,\mathrm{m^3\,kg^{-1}}\times E_{endft}^{-1})$, inversely proportional to E_{endft}.

B.2.2. Time-dependent solution of the lumped-parameter model in the absence of the valve

In complex domain equation (4.1) can be written as

$$\tilde{q}_{art}\approx 2\pi r_1 lh_{cp}2\pi f\,e^{2\pi ift}.$$ (B 35)

In the absence of the valve, equation (4.3) can be rewritten as

$$2\pi r_1 lh_{cp}2\pi f\,e^{2\pi ift+(t/R_{eff}C_{endft})}=C_{endft}\frac{\partial(pe^{t/R_{eff}C_{endft}})}{\partial t},$$ (B 36)

where $R_{eff}^{-1}=(R_{endft}+R_{ecs})^{-1}+R_{pial}^{-1}$. Integrating equation (B 35) over time, we have

$$\frac{2\pi r_1 lh_{cp}2\pi f}{2\pi fi+(1/R_{eff}C_{endft})}\,e^{2\pi ift+(t/R_{eff}C_{endft})}=C_{endft}p\,e^{t/R_{eff}C_{endft}}.$$ (B 37)

Therefore, we have the analytical solution for the pressure

$$p=\frac{4\pi^2 r_1 lh_{cp}f}{C_{endft}(2\pi fi+(1/R_{eff}C_{endft}))}\,e^{2\pi ift}$$
$$=\frac{4\pi^2 r_1 l\bar{h}_{cp}f\,e^{2\pi i(ft-(\arctan(2\pi fR_{eff}C_{endft})/2\pi))}}{C_{endft}\sqrt{4\pi^2 f^2+(1/R_{eff}C_{endft})^2}}.$$ (B 38)

From equation (B 37), we can derive equation (4.4), given that $p=-R_{pial}\,q_{pial}$.

B.2.3. Solution of the lumped-parameter model in the presence of the valve neglecting the endfoot wall deformation

Neglecting the endfoot wall deformation, equation (4.3) can be rewritten as

$$\frac{p}{R_{eff}}=q_{art},$$ (B 39)

where $R_{eff}^{-1}=(R_{endft}+R_{ecs})^{-1}+R_{pial}^{-1}$. Given that $p=-R_{pial}\,q_{pial}$, we have

$$q_{pial}=-\frac{R_{eff}q_{art}}{R_{pial}}.$$ (B 40)

Since R_{eff} contains R_{endft}, which depends on the pressure and acts like a valve (equation (B 32)), we can therefore calculate the net inflow volume V_{pial} per cycle:

$$V_{pial}=\int_0^{t_*}\frac{R_{eff1}q_{art}}{R_{pial}}\,dt+\int_{t_*}^{t_0}\frac{R_{eff2}q_{art}}{R_{pial}}\,dt,$$ (B 41)

where R_{eff1} is the value of R_{eff} when the artery dilates ($q_{art}>0$) and the valve opens, and R_{eff2} is the value of R_{eff} when the artery constricts ($q_{art}\leq 0$) and the valve closes. Here, t_* is the time when q_{art} changes sign and the valve switches its state, and t_0 is the period of the cycle. Since the artery diameter always returns to the baseline after one cycle, we have $V_{art}=\int_0^{t_0}q_{art}\,dt=0$, or $\int_0^{t_*}q_{art}\,dt=-\int_{t_*}^{t_0}q_{art}\,dt$. We can therefore rewrite equation (B 40) as

$$V_{pial}=\gamma\int_0^{t_*}q_{art}\,dt=|\gamma|\int_0^{t_*}|q_{art}|\,dt=\frac{\gamma}{2}|\int_0^{t_0}|q_{art}|\,dt,$$ (B 42)

where $\gamma=(R_{eff2}/R_{pial})-(R_{eff1}/R_{pial})>0$. The second equality in equation (B 41) holds because the sign of q_{art} is consistently positive during the time range of integration (the dilation period). The third equality holds because $\int_0^{t_0}|q_{art}|\,dt=\int_{t_*}^{t_0}|q_{art}|\,dt$.

References

1. Bohr T et al. 2022 The glymphatic system: current understanding and modeling. iScience 25, 104987. (doi:10.1016/j.isci.2022.104987)

2. Kelley DH, Thomas JH. 2023 Cerebrospinal fluid flow. Annu. Rev. Fluid Mech. 55, 237–264. (doi:10.1146/annurev-fluid-120720-011638)

3. Bedussi B, Almasian M, de Vos J, VanBavel E, Bakker EN. 2017 Paravascular spaces at the brain surface: low resistance pathways for cerebrospinal fluid flow. J. Cereb. Blood Flow Metabol. 38, 719–726. (doi:10.1177/0271678X17737984)

4. Mestre H et al. 2018 Flow of cerebrospinal fluid is driven by arterial pulsations and is reduced in hypertension. Nat. Commun. 9, 4878. (doi:10.1038/s41467-018-07318-3)

5. Raghunandan A, Ladron-de Guevera A, Tithof J, Mestre H, Du T, Nedergaard M, Thomas JH, Kelley DH. 2018 Bulk flow of cerebrospinal fluid observed in periarterial spaces is not an artifact of injection. eLife 10, e65958. (doi:10.7554/eLife.65958)

6. Hadaczek P, Yamashita Y, Mirek H, Tamas L, Bohn MC, Noble C, Park JW, Bankiewicz K. 2006 The 'perivascular pump' driven by arterial pulsation is a powerful mechanism for the distribution of therapeutic molecules within the brain. Mol. Ther. 14, 69–78. (doi:10.1016/j.ymthe.2006.02.018)

7. Wang P, Olbricht WL. 2011 Fluid mechanics in the perivascular space. J. Theor. Biol. 274, 52–57. (doi:10.1016/j.jtbi.2011.01.014)

8. Carr JB, Thomas JH, Liu J, Shang JK. 2021 Peristaltic pumping in thin non-axisymmetric annular tubes. J. Fluid Mech. 917, A10. (doi:10.1017/jfm.2021.277)

9. Kedarasetti RT, Drew PT, Costanzo F. 2020 Arterial pulsations drive oscillatory flow of CSF but not directional pumping. Sci. Rep. 10, 10102. (doi:10.1038/s41598-020-66887-w)

10. Daversin-Catty C, Vinje V, Mardal KA, Rognes ME. 2020 The mechanisms behind perivascular fluid flow. PLoS ONE 15, e0244442. (doi:10.1371/journal.pone.0244442)

11. van Veluw SJ, Hou SS, Calvo-Rodriguez M, Arbel-Ornath M, Snyder AC, Frosch MP, Greenberg SM, Bacskai BJ. 2020 Vasomotion as a driving force for paravascular clearance in the awake mouse brain. Neuron 105, 549–561.e5. (doi:10.1016/j.neuron.2019.10.033)

12. Kedarasetti RT, Drew PJ, Costanzo F. 2022 Arterial vasodilation drives convective fluid flow in the brain: a poroelastic model. Fluids Barriers CNS 19, 34. (doi:10.1186/s12987-022-00326-y)

13. Holstein-Rønsbo S et al. 2023 Glymphatic influx and clearance are accelerated by neurovascular coupling. Nat. Neurosci. 26, 1042–1053. (doi:10.1038/s41593-023-01327-2)

14. Bork PAR, Ladrón-de Guevara A, Christensen AH, Jensen KH, Nedergaard M, Bohr T. 2023 Astrocyte endfeet may theoretically act as valves to convert pressure oscillations to glymphatic flow. J. R. Soc. Interface 20, 20230050. (doi:10.1098/rsif.2023.0050)

15. Ray LA, Heys JJ. 2019 Fluid flow and mass transport in brain tissue. Fluids 4, 196. (doi:10.3390/fluids4040196)

16. Wang MX, Ray L, Tanaka KF, Iliff JJ, Heys J. 2021 Varying perivascular astroglial endfoot dimensions along the vascular tree maintain perivascular-interstitial flux through the cortical mantle. Glia 69, 715–728. (doi:10.1002/glia.23923)

17. Asgari M, de Zélicourt D, Kurtcuoglu V. 2016 Glymphatic solute transport does not require bulk flow. Sci. Rep. 6, 38635. (doi:10.1038/srep38635)

18. Diem AK, MacGregor Sharp M, Gatherer M, Bressloff NW, Carare RO, Richardson G. 2017 Arterial pulsations cannot drive intramural periarterial drainage: significance for Aβ drainage. Front. Neurosci. 11, 353–359. (doi:10.3389/fnins.2017.00475)

19. Diem AK, Tan M, Bressloff NW, Hawkes C, Morris AW, Weller RO, Carare RO. 2016 A simulation model of periarterial clearance of amyloid-β from the brain. Front. Aging Neurosci. 8, 18. (doi:10.3389/fnagi.2016.00018)

20. Romanò F, Suresh V, Galie PA, Grotberg JB. 2020 Peristaltic flow in the glymphatic system. Sci. Rep. 10, 21065. (doi:10.1038/s41598-020-77787-4)

21. Kedarasetti RT, Turner KL, Echagarruga C, Gluckman BJ, Drew PJ, Costanzo F. 2020 Functional hyperemia drives fluid exchange in the paravascular space. Fluids Barriers CNS 17, 52. (doi:10.1186/s12987-020-00214-3)

22. Xie L et al. 2013 Sleep drives metabolite clearance from the adult brain. Science 342, 373–377. (doi:10.1126/science.1241224)

23. Iliff J, Wang M, Zeppenfeld D, Venkataraman A, Plog B, Liao Y, Deane R, Nedergaard M. 2013 Cerebral arterial pulsation drives paravascular CSF-interstitial fluid exchange in the murine brain. J. Neurosci. 33, 18 190–18 199. (doi:10.1523/JNEUROSCI.1592-13.2013)

24. Kress B et al. 2014 Impairment of paravascular clearance pathways in the aging brain. Ann. Neurol. 76, 845–861. (doi:10.1002/ana.24271)

25. Schreder HE, Liu J, Kelley DH, Thomas JH, Boster KAS. 2022 A hydraulic resistance model for interstitial fluid flow in the brain. J. R. Soc. Interface 19, 20210812. (doi:10.1098/rsif.2021.0812)

26. Min Rivas F, Liu J, Martell BC, Du T, Mestre H, Nedergaard M, Tithof J, Thomas JH, Kelley DH. 2020 Surface periarterial spaces of the mouse brain are open, not porous. J. R. Soc. Interface 17, 20200593. (doi:10.1098/rsif.2020.0593)

27. Tithof J, Boster KA, Bork PA, Nedergaard M, Thomas JH, Kelley DH. 2022 A network model of glymphatic flow under different experimentally-motivated parametric scenarios. iScience 25, 104258. (doi:10.1016/j.isci.2022.104258)

28. Koch T, Vinje V, Mardal KA. 2022 Estimates for the astrocyte endfoot sheath permeability of the extra-cellular pathway. bioRxiv. (doi:10.1101/2022.11.16.516727)

29. Boster KAS, Tithof J, Cook DD, Thomas JH, Kelley DH. 2022 Sensitivity analysis on a network model of glymphatic flow. J. R. Soc. Interface 19, 20220257. (doi:10.1098/rsif.2022.0257)

30. Holter KE et al. 2017 Interstitial solute transport in 3D reconstructed neuropil occurs by diffusion rather than bulk flow. Proc. Natl Acad. Sci. USA 114, 9894–9899. (doi:10.1073/pnas.1706942114)

31. Neeves K, Lo C, Foley C, Saltzman W, Olbricht W. 2006 Fabrication and characterization of microfluidic probes for convection enhanced drug delivery. J. Control. Release 111, 252–262. (doi:10.1016/j.jconrel.2005.11.018)

32. Smith JH, Humphrey JA. 2007 Interstitial transport and transvascular fluid exchange during infusion into brain and tumor tissue. Microvasc. Res. 73, 58–73. (doi:10.1016/j.mvr.2006.07.001)

33. Bojarskaite L, Vallet A, Bjørnstad DM, Gullestad Binder KM, Cunen C, Heuser K, Kuchta M, Mardal KA, Enger R. 2023 Sleep cycle-dependent vascular dynamics in male mice and the predicted effects on perivascular cerebrospinal fluid flow and solute transport. Nat. Commun. 14, 953. (doi:10.1038/s41467-023-36643-5)

34. Messas E, Pernot M, Couade M. 2013 Arterial wall elasticity: state of the art and future prospects. Diagn. Interv. Imaging 94, 561–569. (doi:10.1016/j.diii.2013.01.025)

35. Boster KA et al. 2023 Artificial intelligence velocimetry reveals in vivo flow rates, pressure gradients, and shear stresses in murine perivascular flows. Proc. Natl Acad. Sci. USA 120, e2217744120. (doi:10.1073/pnas.2217744120)

36. Hablitz LM, Vinitsky HS, Sun Q, Stæger FF, Sigurdsson B, Mortensen KN, Lilius TO, Nedergaard M. 2019 Increased glymphatic influx is correlated with high EEG delta power and low heart rate in mice under anesthesia. Sci. Adv. 5, eaav5447. (doi:10.1126/sciadv.aav5447)

37. Avrahami I, Gharib M. 2008 Computational studies of resonance wave pumping in compliant tubes. J. Fluid Mech. 608, 205–222. (doi:10.1017/S0022112008002012)

38. Penn RD, Linninger A. 2009 The physics of hydrocephalus. Pediatr. Neurosurg. 45, 161–174. (doi:10.1159/000218198)

39. Thomas JH. 2019 Theoretical analysis of wake/sleep changes in brain solute transport suggest a flow of interstitial fluid. Fluids Barriers CNS 19, 30. (doi:10.1186/s12987-022-00325-z)

40. Nicholson C, Hrabětová S. 2017 Brain extracellular epace: the final frontier of neuroscience. Biophys. J. 113, 2133–2142. (doi:10.1016/j.bpj.2017.06.052)

41. Adams MD, Winder AT, Blinder P, Drew PJ. 2018 The pial vasculature of the mouse develops according to a sensory-independent program. Sci. Rep. 8, 9860. (doi:10.1038/s41598-018-27910-3)

42. Greiner A, Reiter N, Paulsen F, Holzapfel GA, Steinmann P, Comellas E, Budday S. 2021 Poro-viscoelastic effects during biomechanical testing of human brain tissue. Front. Mech. Eng. 7, 708350. (doi:10.3389/fmech.2021.708350)

43. Lu YB et al. 2006 Viscoelastic properties of individual glial cells and neurons in the CNS. Proc. Natl Acad. Sci. USA 103, 17 759–17 764. (doi:10.1073/pnas.0606150103)

44. Benveniste H, Liu X, Koundal S, Sanggaard S, Lee H, Wardlaw J. 2019 The glymphatic system and waste clearance with brain aging: a review. *Gerontology* **65**, 106–119. (doi:10.1159/000490349)

45. Mestre H *et al.* 2018 Aquaporin-4-dependent glymphatic solute transport in the rodent brain. *eLife* **7**, e40070. (doi:10.7554/eLife.40070)

46. Mestre H, Kostrikov S, Mehta R, Nedergaard M. 2017 Perivascular spaces, glymphatic dysfunction, and small vessel disease. *Clin. Sci.* **131**, 2257–2274. (doi:10.1042/CS20160381)

47. Mestre H *et al.* 2022 Periarteriolar spaces modulate cerebrospinal fluid transport into brain and demonstrate altered morphology in aging and Alzheimer's disease. *Nat. Commun.* **13**, 3897. (doi:10.1038/s41467-022-31257-9)

48. Tithof J, Kelley DH, Mestre H, Nedergaard M, Thomas JH. 2019 Hydraulic resistance of periarterial spaces in the brain. *Fluids Barriers CNS* **16**, 19. (doi:10.1186/s12987-019-0140-y)

49. Thomas JH. 2019 Fluid dynamics of cerebrospinal fluid flow in perivascular spaces. *J. R. Soc. Interface* **16**, 52–57. (doi:10.1098/rsif.2019.0572)

50. Iliff J *et al.* 2012 A paravascular pathway facilitates CSF flow through the brain parenchyma and the clearance of interstitial solutes, including amyloid β. *Sci. Transl. Med.* **4**, 147ra111. (doi:10.1126/scitranslmed.3003748)

51. Zhao Y, Gan Y, Kelley D, Holstein-Rønsbo S, Boster K, John T, Nedergaard M. Perivascular pumping of cerebrospinal fluid in the brain with a valve mechanism (Version 0.230822.1616) [Data set]. *DANDI archive*. (doi:10.48324/dandi.000547/0.230822.1616)